Lateral Stability Control of In-Wheel-Motor-Driven Electric Vehicles Based on Sideslip Angle Estimation Using Lateral Tire Force Sensors

Kanghyun Nam, *Student Member, IEEE*, Hiroshi Fujimoto, *Member, IEEE*, and Yoichi Hori, *Fellow, IEEE*

***Abstract*—This paper presents a method for using lateral tire force sensors to estimate vehicle sideslip angle and to improve vehicle stability of in-wheel-motor-driven electric vehicles (IWM-EVs). Considering that the vehicle motion is governed by tire forces, lateral tire force measurements give practical benefits in estimation and motion control. To estimate the vehicle sideslip angle, a state observer derived from the extended-Kalman-filtering (EKF) method is proposed and evaluated through field tests on an experimental IWM-EV. Experimental results show the ability of a proposed observer to provide accurate estimation. Moreover, using the estimated sideslip angle and tire cornering stiffness, the vehicle stability control system, making best use of the advantages of IMW-EVs with a steer-by-wire system, is proposed. Computer simulation using Matlab/Simulink-Carsim and experiments are carried out to demonstrate the effectiveness of the proposed stability control system. Practical application of lateral tire force sensors to vehicle control systems is discussed for future personal electric vehicles.**

***Index Terms*—In-wheel-motor-driven electric vehicle (IWM-EV), lateral stability control, lateral tire force sensor, sideslip angle estimation.**

NOMENCLATURE

a_y	Lateral acceleration at center of gravity (CG).
d	Track width.
i	1, 2, 3, and 4 corresponding to front left, front right, rear left, and rear right $(= \mathrm{fl}, \mathrm{fr}, \mathrm{rl}, \mathrm{rr})$.
l	Distance from front axle to rear axle.
l_f	Distance from CG to front axle.
l_r	Distance from CG to rear axle.
r	Wheel nominal radius.
v_x	Longitudinal velocity at CG.
v_y	Lateral velocity at CG.
m	Total mass of vehicle.
C_i	Tire cornering stiffness at the ith tire.
C_f	Front tire cornering stiffness.
C_r	Rear tire cornering stiffness.
C_{fl}	Tire cornering stiffness of the front-left tire.
C_{fr}	Tire cornering stiffness of the front-right tire.
F_i^x	Longitudinal tire force at the ith tire.
F_{fl}^x	Longitudinal force acting on the front-left tire.
F_{fr}^x	Longitudinal force acting on the front-right tire.
F_{rl}^x	Longitudinal force acting on the rear-left tire.
F_{rr}^x	Longitudinal force acting on the rear-right tire.
F_i^y	Lateral tire force at the ith tire.
F_f^y	Front lateral tire force $(= F_{\mathrm{fl}}^y + F_{\mathrm{fr}}^y)$.
F_r^y	Rear lateral tire force $(= F_{\mathrm{rl}}^y + F_{\mathrm{rr}}^y)$.
F_{fl}^y	Lateral force acting on the front-left tire.
F_{fr}^y	Lateral force acting on the front-right tire.
F_{rl}^y	Lateral force acting on the rear-left tire.
F_{rr}^y	Lateral force acting on the rear-right tire.
I_z	Yaw moment of inertia.
I_ω	Wheel angular moment of inertia.
M_z	Yaw moment.
T_{cmd}	Torque command from acceleration pedal.
T_i^m	In-wheel motor torque applied to the ith tire.
T_{rl}^m	Rear-left in-wheel motor torque.
T_{rr}^m	Rear-right in-wheel motor torque.
α_i	Tire slip angle at the ith tire.
α_f	Front-tire slip angle.
α_r	Rear-tire slip angle.
β	Vehicle sideslip angle.
β_d	Desired vehicle sideslip angle.
$\hat{\beta}$	Estimated sideslip angle.
δ_{cmd}	Driver's steering angle command.
δ_f	Front steering angle.
γ	Yaw rate.
γ_d	Desired yaw rate.
λ	Forgetting factor.
μ	Road friction coefficient.
ω_i	Wheel angular velocity at the ith tire.

Manuscript received June 24, 2011; revised November 14, 2011 and January 31, 2012; accepted March 9, 2012. Date of publication March 21, 2012; date of current version June 12, 2012. This work was supported in part by the Industrial Technology Research Grant Program from New Energy and Industrial Technology Development Organization of Japan. The review of this paper was coordinated by Prof. J. Wang.

K. Nam is with the Department of Electrical Engineering, Graduate School of Engineering, The University of Tokyo, Tokyo 113-8656, Japan (e-mail: nam@hori.k.u-tokyo.ac.jp).

H. Fujimoto and Y. Hori are with the Department of Advanced Energy, Graduate School of Frontier Sciences, The University of Tokyo, Chiba 277-8561, Japan (e-mail: fujimoto@k.u-tokyo.ac.jp; hori@k.u-tokyo.ac.jp).

Color versions of one or more of the figures in this paper are available online at http://ieeexplore.ieee.org.

Digital Object Identifier 10.1109/TVT.2012.2191627

I. INTRODUCTION

ELECTRIC vehicles equipped with in-wheel motors have appeared as future personal electric vehicles based on several advantages in the viewpoint of energy efficiency and motion control. Over the past few years, a great deal of research on motion controls, including traction control or yaw stability control, has been done utilizing independently driven in-wheel motors [1]–[3]. The purpose of these motion controls is to

prevent unintended vehicle behavior through active vehicle control and assist drivers in maintaining the controllability and stability of vehicles. The main goal of most motion control systems is to control the sideslip angle and yaw rate of the vehicles. In [4], direct yaw moment control based on sideslip angle estimation was proposed for improving the stability of in-wheel-motor-driven electric vehicles (IWM-EVs). Fuzzy-rule-based control and sliding-mode control algorithms for vehicle stability enhancement were proposed and evaluated through experiments [5], [6]. In vehicle stability control systems, it is required to accurately measure yaw rate and sideslip angle. The yaw rate information is easily obtained by using low-cost gyro sensors. However, a vehicle sideslip angle cannot be directly measured due to expensive sensors, and thereby, it is estimated using available sensors (e.g., gyro sensors, acceleration sensors, steering angle sensors, etc.) and vehicle models. Recently, several methods for estimating vehicle sideslip angle have been extensively studied [8]–[12]. A new methodology of combining a vehicle-model-based method and a kinematics-based method was proposed and evaluated by experiments in [8]. In [10], nonlinear techniques for estimating lateral tire forces and sideslip angle, using extended and unscented Kalman filters (KFs), were proposed and evaluated by field tests. A nonlinear observer based on a double-track vehicle model is designed and validated with real measurement data [11]. In [12], an observer based on forcing the dynamics of the nonlinear estimation error to follow the linear dynamics is presented.

An estimation approach using Global Positioning System (GPS) measurements was presented to overcome some of the drawbacks of conventional methods (e.g., vehicle-model- and kinematics-based methods) [13], [14]. However, GPS-based estimation methods require satellite visibility, which is periodically lost in urban and forested areas. To overcome these difficulties in accurate and robust estimation, the research team in [24] and [25] has applied lateral tire force sensors to state estimation.

Motion control systems for electric vehicles, which are known as yaw stability control or vehicle stability control, are mostly realized by independent in-wheel motor control [3]–[7]. In [17] and [18], active steering control methods for vehicle motion control were proposed and demonstrated through experiments. The potential benefits of active steering control through a steer-by-wire (SbW) system to improve handling behaviors during normal driving have received considerable attention from the automobile industry. A robust yaw stability control method based on a 2 degree-of-freedom (2-DOF) steering control architecture was presented, and its effectiveness was verified using a hardware-in-the-loop simulation setup [15] and field tests [16]. By utilizing active steering control via an SbW system, it is possible to realize the desired vehicle motion without causing uncomfortable driver feeling. In [19], an adaptive nonlinear control scheme, which is aimed at the improvement of the handling properties of vehicles, was proposed based on active steering control and wheel torque control. A vehicle motion control method based on a yaw moment observer and a lateral force observer is proposed and compared with a conventional decoupling control method [20].

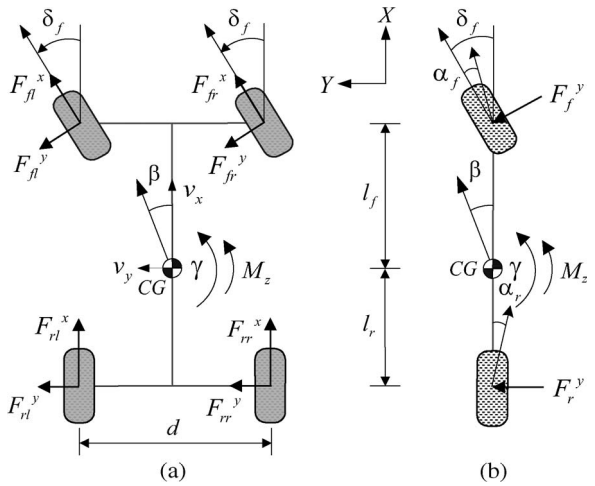

Fig. 1. Planar vehicle model. (a) Four-wheel model. (b) Single-track model (i.e., bicycle model).

In this paper, a new sideslip angle observer derived from extended KF (EKF) techniques is proposed based on the use of lateral tire force sensors. To evaluate the benefits of the proposed observer, the estimation results are compared with the results of a kinematics-based method [24]. In field tests, an IWM-EV developed by the authors' research team was used. Using the estimated state and parameter, the stability control system, which is based on active steering control and an independent in-wheel motor control scheme, is proposed, and its control performances are verified through computer simulation and experiments. Active front steering control is applied for sideslip angle control; on the other hand, independent rear in-wheel motor control is applied for yaw rate control. A 2-DOF scheme based on the adaptive feed-forward control method is used for stability controller design. An adaptive feedforward controller is designed using estimated tire cornering stiffness. The remainder of this paper is organized as follows: In Section II, vehicle modeling and dynamic tire modeling are presented. Section III introduces the experimental IWM-EV that was developed by our research team. Section IV describes the proposed sideslip angle observer and tire cornering stiffness estimation methods using lateral tire force sensors, which was proposed in [27]. Section V presents the vehicle stability control system. In Section VI, simulation and experimental results are presented and discussed. Finally, we make a conclusion regarding our research and future works.

II. Vehicle and Tire Modeling

A. Vehicle Modeling

In this section, a yaw plane model is introduced to describe the motion of an IWM-EV. Although the modeling method describing the 3-D vehicle motion [28], [29] is used for observer or control design, in this study, the vehicle motion on yaw plane is only considered. The main difference with the commonly used vehicle dynamics model is that the direct yaw moment can be an additional input variable, which is generated by motor torque difference between each wheel. The yaw plane representation is shown in Fig. 1.

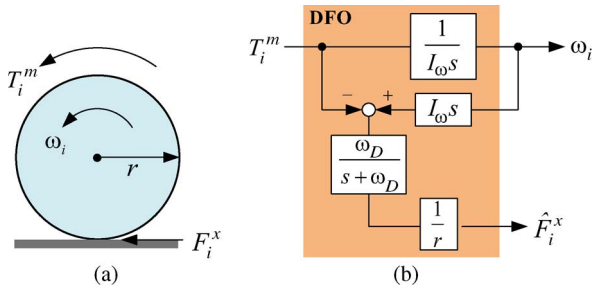

Fig. 2. (a) Wheel rotational motion. (b) Block diagram of a DFO [22].

The equation of motion governing the lateral dynamics of the four wheel model, as shown in Fig. 1(a), is given by

$$mv_x(\dot{\beta}+\gamma) = \sum_{i=1}^{2}\left(F_i^x \sin\delta_f + F_i^y \cos\delta_f\right) + \sum_{i=3}^{4}\left(F_i^y\right). \quad (1)$$

The yaw moment balance equation with respect to CG is

$$I_z\dot{\gamma} = \sum_{i=1}^{2} l_f\left(F_i^x \sin\delta_f + F_i^y \cos\delta_f\right) - \sum_{i=3}^{4} l_r\left(F_i^y\right) + M_z \quad (2)$$

where the yaw moment M_z is a direct yaw moment input, which is induced by independent torque control of in-wheel motors and can be calculated as follows:

$$M_z = \frac{d}{2}\left(F_{\mathrm{rr}}^x - F_{\mathrm{rl}}^x\right) + \frac{d}{2}\left(F_{\mathrm{fr}}^x - F_{\mathrm{fl}}^x\right)\cos\delta_f. \quad (3)$$

Here, the longitudinal tire forces, i.e., F_{rl}^x and F_{rr}^x, can be obtained from a driving force observer (DFO), which is designed based on wheel rotational motion [22], [23]. Several researchers have proposed the methods for longitudinal tire force estimation. In [28], a sliding-mode observer has been developed to estimate the longitudinal tire forces, and its effectiveness is experimentally verified. In this paper, the longitudinal tire forces are estimated by using the wheel angular velocity; the in-wheel motor torque, which is easily measured from the motor current; and the rotational wheel dynamics (see Fig. 2). The longitudinal tire force observer is designed as [22]

$$\hat{F}_i^x = \frac{\omega_D}{s+\omega_D}\left(\frac{T_i^m - I_\omega\omega_i s}{r}\right) \quad (4)$$

where the angular velocity of the wheel ω_i is measured; the in-wheel motor torque T_i^m is measured from the motor current; ω_D is a cutoff frequency of the applied low-pass filter, which rejects high-frequency noises caused by the time derivative of ω_i; and $\hat{F}_i^x$ is the estimated longitudinal tire force. Note that the DFO shown in Fig. 2(b) is quite similar to the well-known disturbance observer structure.

For design simplicity, the single-track model, as shown in Fig. 1(b), is used in observer and controller design. From this model, the lateral and yaw dynamics are simplified as

$$mv_x(\dot{\beta}+\gamma) = F_f^y\cos\delta_f + F_r^y \quad (5)$$

$$I_z\dot{\gamma} = l_f F_f^y\cos\delta_f - l_r F_r^y + M_z. \quad (6)$$

For small tire slip angles, the lateral tire forces can be linearly approximated as follows:

$$F_f^y = -2C_f\left(\beta + \frac{\gamma l_f}{v_x} - \delta_f\right), \qquad F_r^y = -2C_r\left(\beta - \frac{\gamma l_r}{v_x}\right). \quad (7)$$

From (5)–(7) with small angle approximation (i.e., $\cos\delta_f \approx 1$), the following state space equation is obtained:

$$\dot{x}(t) = Ax(t) + Bu(t)$$
$$y(t) = Cx(t) \quad (8)$$

where $x = [\beta, \gamma]^T$, $u = [\delta_f, M_z]^T$, $y = \gamma$, and

$$A = \begin{bmatrix} \frac{-2(C_f+C_r)}{mv_x} & \frac{-2(l_fC_f - l_rC_r)}{mv_x^2} - 1 \\ \frac{-2(l_fC_f - l_rC_r)}{I_z} & \frac{-2\left(l_f^2C_f + l_r^2C_r\right)}{I_z v_x} \end{bmatrix}$$

$$B = \begin{bmatrix} \frac{2C_f}{mv_x} & 0 \\ \frac{2l_fC_f}{I_z} & \frac{1}{I_z} \end{bmatrix}, \quad C = [0 \quad 1].$$

Here, we can see that there are two states to be controlled and two controllable inputs. Moreover, it is found that that the variations of vehicle longitudinal velocity v_x cause noticeable changes in vehicle dynamic responses. That is, a damping coefficient and natural frequency of the vehicle dynamics model, which are defined in Appendix A, dominantly depend on vehicle longitudinal velocity. Thus, proper gain-scheduling strategies based on vehicle longitudinal velocity are required in control system design. It is customary to design controllers for several velocity values and to use a gain-scheduling controller [15].

B. Dynamic Lateral Tire Force Model

The tires, which generate longitudinal, lateral forces and moments, have a significant effect on the dynamic characteristics of vehicles. These tire forces are explained by a complex relation among tire–road friction, normal force on the tire, variable slip angles, and elastic tire properties. To model tire force generation, several tire models have been developed. A widely used empirical tire model (e.g., magic formula tire model) is dominantly based on empirical formulations deriving from tire test data and a large number of tire parameters. In this paper, to avoid complex calculation, dependence on tire parameters, and use of tire test data, the linearized tire force model is used, as shown in (7). Moreover, to account for the transient behavior of tires, a typical dynamic tire model, which is the first-order dynamics, is used and expressed as follows [34]:

$$\tau_{\mathrm{lag},i}\dot{F}_i^y + F_i^y = \bar{F}_i^y \quad (9)$$

where $\tau_{\mathrm{lag},i}$ is the relaxation time constant and is calculated from the longitudinal vehicle velocity and tire relaxation length, which is the approximate distance needed to build up tire forces; and $\bar{F}_i^y$ is the lateral tire force from a linear tire

Fig. 3. Experimental IMW-EV.

(a) (b)

Fig. 4. (a) In-wheel motor. (b) MSHub unit.

model described in (7). From (7) and (9), the dynamic lateral tire force models for front and rear tires are obtained as follows:

$$\dot{F}_f^y = -\frac{1}{\tau_{\mathrm{lag},f}}F_f^y - \frac{2C_f}{\tau_{\mathrm{lag},f}}\beta - \frac{2l_fC_f}{\tau_{\mathrm{lag},f}v_x}\gamma + \frac{2C_f}{\tau_{\mathrm{lag},f}}\delta_f \quad (10)$$

$$\dot{F}_r^y = -\frac{1}{\tau_{\mathrm{lag},r}}F_r^y - \frac{2C_r}{\tau_{\mathrm{lag},r}}\beta + \frac{2l_rC_r}{\tau_{\mathrm{lag},r}v_x}\gamma \quad (11)$$

where $\tau_{\mathrm{lag},f}$ and $\tau_{\mathrm{lag},r}$ are the relaxation time constants for front and rear tires, respectively (e.g., $\tau_{\mathrm{lag},f} = 0.053$ s and $\tau_{\mathrm{lag},r} = 0.065$ s, which are chosen from measured sensor data).

III. Experimental Electric Vehicle

To implement and verify the proposed state observer and stability control system, an IWM-EV (see Fig. 3), which was developed by the Hori/Fujimoto research team, was used. In-wheel motors, which are shown in Fig. 4(a), are mounted in each wheel. Therefore, we can completely and independently control each wheel's torque. Regenerative braking is also available. Moreover, active front-steering control is possible through an SbW system.

The most outstanding feature of the experimental IWM-EV is that lateral tire force sensors [called multisensing hub (MSHub) units shown in Fig. 4(b)], which were invented by NSK Ltd. [37], are installed in each wheel to measure lateral tire forces in real time. By directly using lateral tire forces, we can accurately estimate vehicle states. In addition, the heuristic and complicated tire models are not required in estimator and control design. MSHub units, including rolling bearings used to support the wheels of the vehicle, can measure the loads applied to the rolling bearing. In many conventional vehicles, wheel hub units with built-in active antilock brake system sensors (i.e., wheel velocity sensor) were equipped. Comparing MSHub units with conventional wheel hub units, which are currently used in many commercial vehicles, MSHub units have almost the same mechanical structure, except for rolling elements in a pair of rows, and are capable of being constructed at a significantly low cost. The measurement principle is given as follows: The revolution speeds of rolling elements in a pair of rows are sensed by a pair of revolution speed sensors, and the difference of sensed revolution speeds is used to calculate the radial or axial loads [37]. Therefore, accurate lateral tire force measurements using MSHub units can be realized without much additional cost. The use of lateral tire force sensors in vehicle motion control systems is able to provide the following advantages.

1) Tire–road conditions can be easily predicted, e.g., during cornering, we can predict the tire–road conditions based on the estimated tire cornering stiffness.
2) Optimal tire force distribution is realizable using lateral tire force measurements and estimated driving forces.
3) Vehicle motion can be controlled at the tire force control level.

An experimental IWM-EV is also equipped with a gyro and acceleration sensors that measure yaw rate, longitudinal, and lateral acceleration. In addition, a noncontact optical sensor, Correvit (Corrsys-Datron), is used for accurate measurements of sideslip angle, lateral vehicle velocity, and longitudinal vehicle velocity. The Correvit sensor uses optical means to capture planar road texture and evaluate the motion of the vehicle by measuring the direction and magnitude of change with respect to the road texture. It should be noted that noncontact optical sensors are very expensive, e.g., the sensors by Corrsys-Datron cost more than $30 000. In this paper, it is only used as a reference for validating the proposed estimation algorithm. The dSPACE AutoBox (DS1103), which consists of a power PC 750GX controller board running at 933 MHz, 16-channel analog-to-digital converter, and 8-channel digital-to-analog converter, was used for real-time data acquisition and control.

IV. Vehicle Sideslip Angle Estimation

A. Tire Cornering Stiffness Estimation

In this paper, a single-track vehicle model (i.e., bicycle model) is used for state estimation and stability control. This vehicle model includes the so-called tire cornering stiffness, which describes the tire–road condition and is a time-varying parameter. In general, there is a significant difference in the value of tire cornering stiffness, depending on the road conditions (e.g., whether the road is dry asphalt or a slippery road), and the value is higher on dry asphalt than on a wet and slippery road. In [26], several methods for cornering stiffness estimation were developed and evaluated using experimental data. In [27], the novel method for cornering stiffness estimation using lateral tire force sensors is proposed. In this paper, using a method proposed in [27], linear tire models, and measured lateral tire forces, we obtain a linear regression model (i.e., the parameter to be identified is C_f/C_r) for tire cornering stiffness estimation. Furthermore, using the following front-left and front-right lat-

eral tire force models (12) and (13), shown below, we can have a regression model (i.e., a parameter to be identified is C_f)

$$F_{\mathrm{fl}}^{y} = -C_{\mathrm{fl}}\left(\frac{v_y+\gamma l_f}{v_x-\gamma d/2}-\delta_f\right) \tag{12}$$

$$F_{\mathrm{fr}}^{y} = -C_{\mathrm{fr}}\left(\frac{v_y+\gamma l_f}{v_x+\gamma d/2}-\delta_f\right) \tag{13}$$

where it is assumed that the tire cornering stiffnesses of the left and right tires are the same (i.e., $C_{\mathrm{fl}} = C_{\mathrm{fr}} \approx C_f$). In general, tire cornering stiffness is affected by weight transfer of vehicles. In contrast to engine vehicles, IWM-EV, having battery packs under the floor and driving motors attached in wheels, can lower the CG of the vehicle. This provides less weight transfer and thereby improves driving stability. From these features, variations in the front-left and front-right tire cornering stiffnesses due to weight transfer are not considered.

The tire cornering stiffness is identified using the following regression model:

$$y(t) = \varphi^T(t)\theta(t) \tag{14}$$

where the parameters to be identified $\theta(t)$, input regression $\varphi^T(t)$, and measured output $y(t)$ are given as [27]

$$y(t) = \begin{bmatrix} F_f^y \\ F_{\mathrm{fr}}^y\left(v_x+\frac{d\gamma}{2}\right)-F_{\mathrm{fl}}^y\left(v_x-\frac{d\gamma}{2}\right)\end{bmatrix}$$

$$\varphi^T(t) = \begin{bmatrix} 2\delta_f-\frac{2\gamma l}{v_x} & F_r^y \\ d\gamma\delta_f & 0\end{bmatrix}, \quad \theta(t) = \begin{bmatrix} C_f \\ \frac{C_f}{C_r}\end{bmatrix}.$$

Tire cornering stiffness in the aforementioned equations is estimated by making use of the recursive least squares (RLS) algorithm as follows [35]:

$$\hat{\theta}[t] = \hat{\theta}[t-1] + \mathrm{Proj}_{\hat{\theta}}\left\{K[t]\left(y[t]-\varphi[t]^T\cdot\hat{\theta}[t-1]\right)\right\}$$

$$K[t] = \frac{P[t-1]\varphi[t]}{\lambda I+\varphi^T[t]P[t-1]\varphi[t]}$$

$$P[t] = \frac{1}{\lambda}\left(I-K[t]\varphi^T[t]\right)P[t-1]$$

$$\mathrm{Proj}_{\hat{\theta}}(\bullet_j) = \begin{cases} 0, & \text{if } \hat{\theta}_j \geq \theta_{j,\max} \text{ and } \bullet_j > 0 \\ 0, & \text{if } \hat{\theta}_j \leq \theta_{j,\min} \text{ and } \bullet_j < 0 \\ \bullet_j, & \text{otherwise}\end{cases} \tag{15}$$

where I is the identity matrix, and $K[t]$ and $P[t]$ are the Kalman gain matrix and covariance matrix, respectively.

In reality, tire cornering stiffness is constrained, depending on the road conditions. This constraint can be enforced by projecting the estimates back into the defined values [i.e., $C_f \in (C_{f,\min}, C_{f,\max}), C_r \in (C_{r,\min}, C_{r,\max})$]. Therefore, the RLS algorithm with discontinuous projection is used [21]. The projection, as shown in (15), is activated when the estimate moves out of the defined parameter extent. Moreover, additional conditions for parameter update are applied. In general, accurate parameter estimation depends on the qualities of the estimator input signal. For example, if the steering angle, yaw rate, and lateral tire forces are very small (e.g., this is a situation of straight driving), the experimental data obtained are then around the zero, where the estimates will be stochastically uncertain. Therefore, to ensure good estimator performance, the parameters (i.e., tire cornering stiffness) are not updated when the absolute values of the steering angle and yaw rate are less than certain small values.

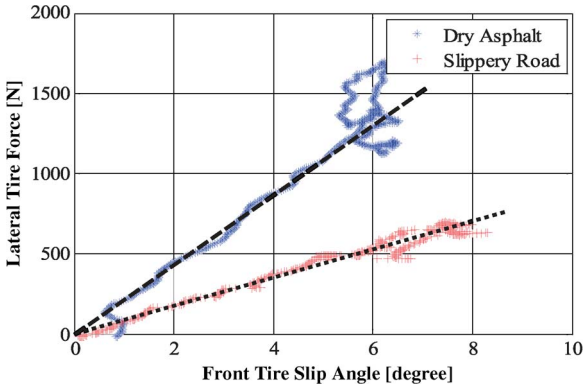

Fig. 5. Lateral tire force measurement–tire slip angle measurement curve.

The extent of tire cornering stiffness is defined from the relationship between sensor measurements (i.e., lateral tire force sensors and sideslip angle sensor) and given by

$$C_f \in (5000, 12500),\ C_r \in (15000, 28500). \tag{16}$$

Field tests under the same driving conditions on dry asphalt and a slippery road were carried out, and those results are shown in Fig. 5. To acquire lateral tire forces ranging from small to large values, the step steering command with a slow angle rate was applied to the IWM-EV on dry asphalt and a slippery road at a constant vehicle speed. Sensor data obtained from lateral tire force sensors and sideslip angle sensors are plotted. The linear behavior between the measured lateral tire force and tire slip angle shows that the lateral tire force is proportional to the tire slip angle in the linear region.

B. Design of Sideslip Angle Observer

In this section, a sideslip angle estimation method, which is based on the use of lateral tire force sensors, is proposed and evaluated through experimental results.

A single-track vehicle model and a dynamic lateral tire force model are used for observer design. The special feature in a proposed observer is that we use the estimated tire cornering stiffness as a measurable state variable. In this paper, the effects of road-bank angle, vehicle roll motion, and suspension deflection are not considered. The nonlinear state space equation, including random walk models for tire cornering stiffness (i.e., $\dot{C}_f = \dot{C}_r = 0$), is expressed as follows:

$$\dot{x}(t) = f\left(x(t), u(t)\right) + \rho(t)$$
$$y(t) = h\left(x(t)\right) + \sigma(t). \tag{17}$$

The state vector x is composed of the vehicle sideslip angle, yaw rate, front lateral tire force, rear lateral tire force, esti-

mated front cornering stiffness, and rear cornering stiffness from (14)

$$\begin{aligned} x &= [\,\beta \quad \gamma \quad F_f^y \quad F_r^y \quad C_f \quad C_r\,]^T \\ &= [\,x_1 \quad x_2 \quad x_3 \quad x_4 \quad x_5 \quad x_6\,]^T. \end{aligned} \tag{18}$$

The measurement vector y is composed of the yaw rate, front and rear lateral tire forces, and estimated front and rear cornering stiffnesses, i.e.,

$$y = [\,\gamma \quad F_f^y \quad F_r^y \quad C_f \quad C_r\,]^T = [\,y_1 \quad y_2 \quad y_3 \quad y_4 \quad y_5\,]^T. \tag{19}$$

The input vector u is composed of the front steering angle and rear left and right driving forces, i.e.,

$$u = [\,\delta_f \quad F_{\mathrm{rl}}^x \quad F_{\mathrm{rr}}^x\,]^T = [\,u_1 \quad u_2 \quad u_3\,]^T \tag{20}$$

where the rear wheels' driving forces are obtained from DFOs shown in Fig. 2. It is noted that an electric vehicle, which is used in field tests, is a rear wheel-driving vehicle, and the rear wheels' driving forces are used as observer inputs.

The process and measurement noise vectors, i.e., $\rho(t)$ and $\sigma(t)$ in (17), are assumed to be of zero mean, white, and uncorrelated. The nonlinear state evolution function $f(x(t), u(t))$ and observation function $h(x(t))$ are expressed as

$$\begin{cases} f_1(x,u) = -x_2 + \frac{\cos u_1}{m v_x} x_3 + \frac{x_4}{m v_x} \\ f_2(x,u) = \frac{l_f \cos u_1 x_3}{I_z} - \frac{l_r x_4}{I_z} - \frac{du_2}{2I_z} + \frac{du_3}{2I_z} \\ f_3(x,u) = -\frac{x_3}{\tau_{\mathrm{lag},f}} - \frac{2x_1x_5}{\tau_{\mathrm{lag},f}} - \frac{2l_f x_2 x_5}{\tau_{\mathrm{lag},f} v_x} + \frac{2x_5 u_1}{\tau_{\mathrm{lag},f}} \\ f_4(x,u) = -\frac{x_4}{\tau_{\mathrm{lag},r}} - \frac{2x_1x_6}{\tau_{\mathrm{lag},r}} + \frac{2l_r x_2 x_6}{\tau_{\mathrm{lag},r} v_x} \\ f_5(x,u) = f_6(x,u) = 0 \end{cases} \tag{21}$$

$$\begin{cases} h_1(x) = x_2, h_2(x) = x_3, h_3(x) = x_4 \\ h_4(x) = x_5, h_5(x) = x_6. \end{cases} \tag{22}$$

Based on the aforementioned nonlinear dynamics, the EKF is designed for sideslip angle estimation. For computer implementation, (17) is discretized by a Euler approximation method and has the following form:

$$\begin{aligned} x_k &= f(x_{k-1}, u_k) + \rho(t) \\ y_k &= h(x_k) + \sigma(t). \end{aligned} \tag{23}$$

The recursive algorithm of first-order EKF is summarized as follows:

1) Initialization: The initial estimation $\hat{x}_0$ before measurement and the initial covariance P_0 are determined by

$$\hat{x}_0 = E[x_0] \quad P_0 = E\left[(x_0 - \hat{x}_0)(x_0 - \hat{x}_0)^T\right]. \tag{24}$$

2) Time Update: In this step, the prediction of the state is carried out based on the state estimate and its covariance from previous time step, i.e.,

$$\begin{aligned} \hat{x}_{k|k-1} &= f(\hat{x}_{k1|k-1}, u_k) \\ P_{k|k-1} &= A_k P_{k1|k-1} A_k^T + Q_\rho \end{aligned} \tag{25}$$

where A_k is the process Jacobian, which is the partial derivative matrix of $f(x_{k-1}, u_k)$ with respect to estimated states, and is given by

$$A_k = \frac{\partial f(\hat{x}_{k-1|k-1}, u_k)}{\partial x}. \tag{26}$$

3) Measurement Update: In this step, the observation vector y_k is used to correct the state estimation and the covariance estimation. The state estimation, KF gain, and estimated covariance are given by

$$\begin{aligned} \hat{x}_{k|k} &= \hat{x}_{k|k-1} + K_k\left[y_k - h(\hat{x}_{k|k-1})\right] \\ K_k &= P_{k|k-1} H_k^T \left[H_k P_{k|k-1} H_k^T + R_\sigma\right]^{-1} \\ P_{k|k} &= [I - K_k H_k] P_{k|k-1} \end{aligned} \tag{27}$$

where H_k is the measurement Jacobian at the kth step of the nonlinear equation with respect to the estimated states and is given by

$$H_k = \frac{\partial h(\hat{x}_{k|k-1})}{\partial x}. \tag{28}$$

In selection of noise covariance matrices (i.e., Q_ρ and R_σ), a diagonal matrix (i.e., individual noise components are not cross correlated) is chosen, and the covariance matrices of process noise and measurement noise are given as follows:

$$Q_\rho = \mathrm{diag}\left[Q_\beta, Q_\gamma, Q_{F_f^y}, Q_{F_r^y}, Q_{C_f}, Q_{C_r}\right] \tag{29}$$

$$R_\sigma = \mathrm{diag}\left[R_\gamma, R_{F_f^y}, R_{F_r^y}, R_{C_f}, R_{C_r}\right]. \tag{30}$$

In covariance matrix setting, it should be noted that the less noise in sensor measurements compared with the uncertainty in dynamics model, the more the states will be adapted to follow sensor measurements. The states (e.g., sideslip angle and yaw rate) are modeled using reliable vehicle dynamics. Therefore, the process noises are relatively small. The suitable process noise variances for lateral tire force models are selected based on comparison with the corresponding measurement noise variances. In case of tire cornering stiffness, new values are much more accurate than the prior states, and thereby, we put the relatively high process uncertainty on it.

C. Experimental Result

The proposed sideslip angle observer was evaluated through field tests. The experimental tests have been done on dry asphalt and wet asphalt, which show normally a high-μ value and a low-μ value, respectively. A pulse steering command is applied to obtain large lateral acceleration (i.e., up to 6 m/s^2), which means that the IWM-EV was put under a critical driving condition. Fig. 6 shows the results of a field test carried out on wet asphalt at $v_x = 50$ km/h. Fig. 6(a) shows the driving conditions, including the steering angle command, lateral acceleration, and yaw rate. According to Fig. 6(b), the proposed observer shows better estimation performance compared with the results of a kinematics-based method (The kinematics-based method was

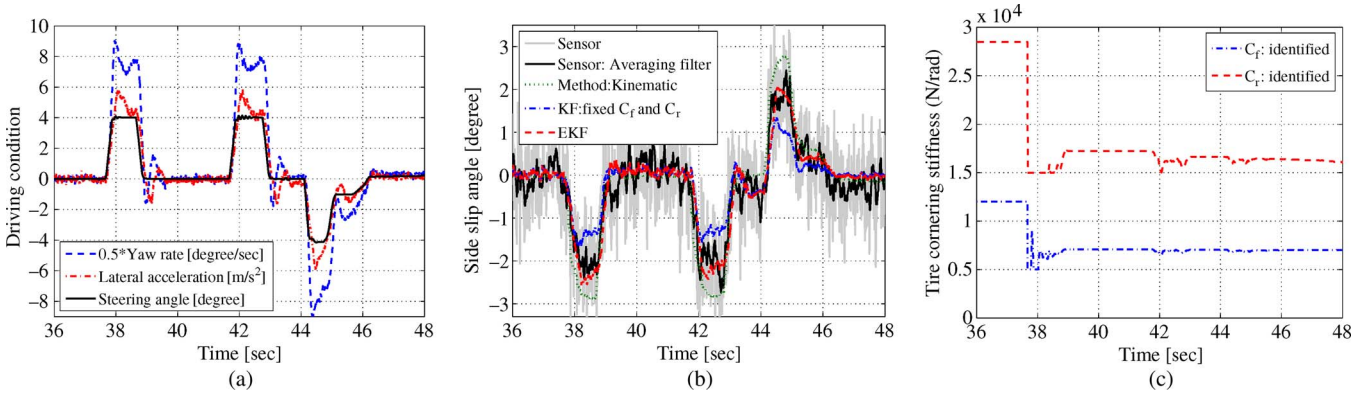

Fig. 6. Estimation result on wet asphalt at $v_x = 50$ km/h. (a) Driving condition. (b) Sideslip angle. (c) Tire cornering stiffness.

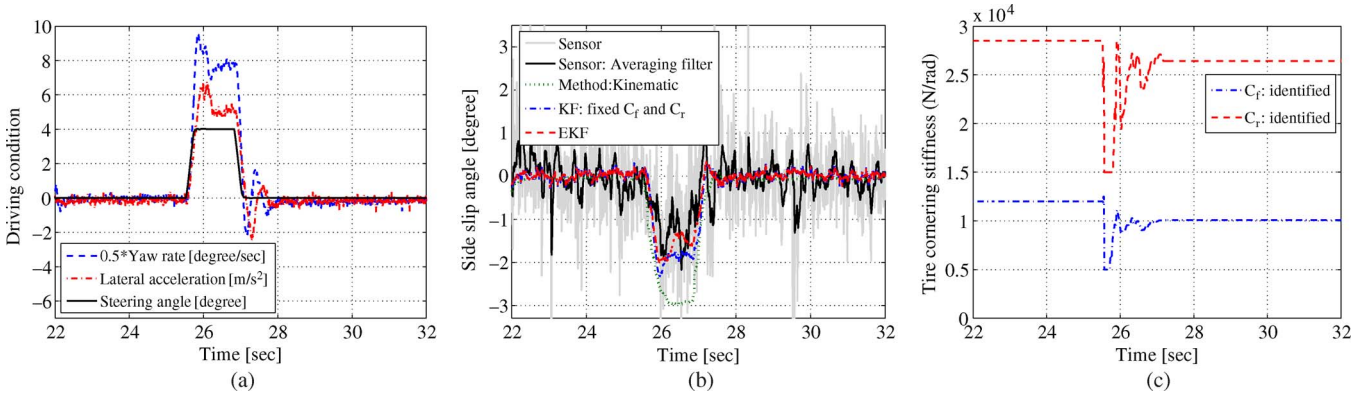

Fig. 7. Estimation result on dry asphalt at $v_x = 55$ km/h. (a) Driving condition. (b) Sideslip angle. (c) Tire cornering stiffness.

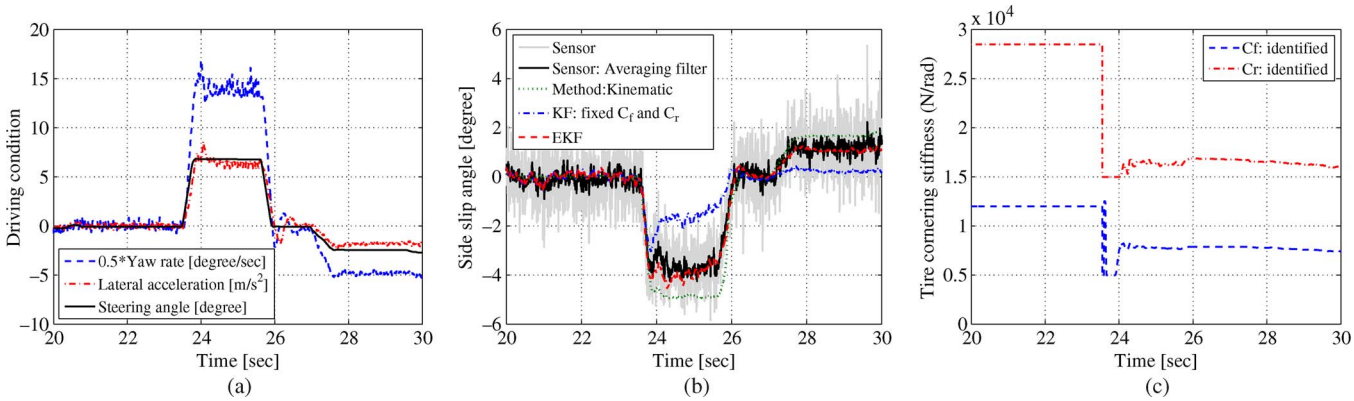

Fig. 8. Estimation result of critical driving (e.g., $|a_y| \simeq 7$ m/s^2) on wet asphalt at $v_x = 60$ km/h. (a) Driving condition. (b) Sideslip angle. (c) Tire cornering stiffness.

proposed by the authors; for further details, see Appendix B and [25].) and a fixed KF method. From Fig. 6(c), we can see that tire cornering stiffness on wet asphalt is much smaller than that on dry asphalt. Therefore, an experimental result of the fixed KF (i.e., this method uses fixed tire cornering stiffness for a value on dry asphalt), as shown in Fig. 6(b), shows a relatively large estimation error. Fig. 7 represents results of a field test on dry asphalt at $v_x = 55$ km/h. According to Fig. 7(b), the proposed observer is relatively good with respect to sensor measurements. Even though there is a small estimation error, this method provides more accurate estimation compared with existing methods. Figs. 6(c) and 7(c) represent the estimation results of tire cornering stiffness obtained from field tests on wet asphalt and dry asphalt, respectively. It can be seen that estimates rapidly converge to final values, which are considered as true tire cornering stiffnesses on each road. In addition, to verify the estimation ability of the proposed observer under more severe driving conditions, we have performed the experiments in a critical driving situation. As shown in Fig. 8(a), the large vehicle lateral acceleration (i.e., absolute value is up to 7 m/s^2) is obtained. This indicates that the tires begin to saturate and reach a peak value; this area is commonly called

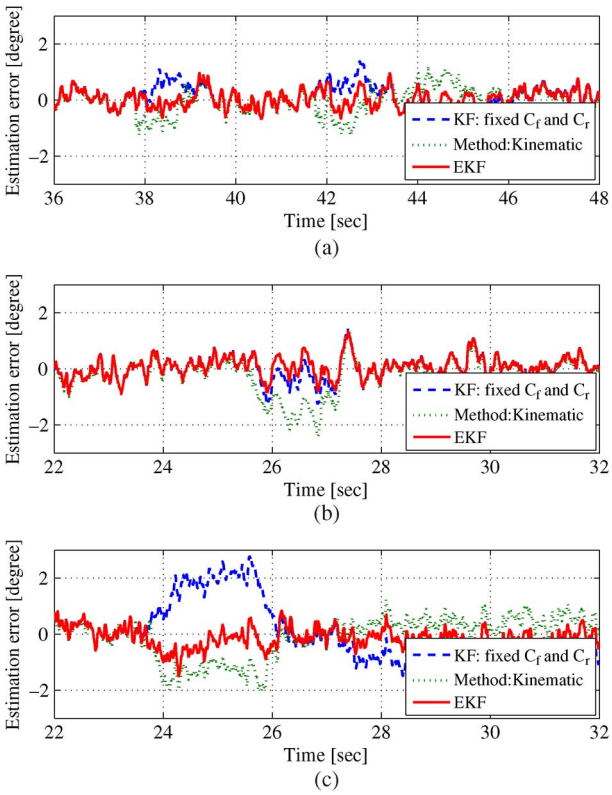

Fig. 9. Estimation error. (a) Result on wet asphalt. (b) Result on dry asphalt. (c) Result of the critical driving on wet asphalt.

the nonlinear tire region. The measurements of the yaw rate and steering angle are also shown in Fig. 8(a). Fig. 8(b) represents the results of the proposed observer and other methods. If we compare the two observers, i.e., KF with fixed C_f and C_r and EKF, we can confirm that the proposed EKF is more efficient and robust against tire–road conditions. Estimation error shown in the result of KF with fixed C_f and C_r is mainly due to the model mismatch caused by varying tire cornering stiffnesses. On the other hand, the proposed EKF shows significantly small estimation error by using estimated tire cornering stiffness. Tire cornering stiffness estimated from an RLS algorithm is shown in Fig. 8(c). Since this experiment was performed on wet asphalt, the results of Fig. 8(c) are very similar to the results of Fig. 6(c).

The estimation error for each method is calculated, i.e., estimation error = sensor measurement − estimate, and its values for three methods are plotted as shown in Fig. 9. Fig. 9(a)–(c) are obtained from the results of Fig. 6–8, respectively. It is shown that the estimation error for the proposed EKF is the smallest, regardless of road conditions. In particular, if we see Fig. 9(c), we can confirm that the estimate from the proposed EKF well follows the real sideslip angle value, even in the critical driving situation. By utilizing the lateral tire force sensors, more accurate and reliable state estimation could be realized without using expensive sideslip angle sensors. Moreover, feasibility of practical application of the lateral tire force sensors to vehicle control systems is verified through experimental results. This is one of the important contributions of this paper.

V. Design of Lateral Stability Control System

In this section, a vehicle lateral stability control system for the IWM-EV is presented, and its effectiveness is evaluated through simulation and experiments. The overall control scheme in Fig. 10 is given as follows.

1) First, the desired vehicle responses are obtained from a linear vehicle model and driver's commands, such as a steering angle and vehicle speed.
2) Second, the lateral stability controller is designed to make the vehicle follow the desired vehicle motion trajectory. The proposed control system has been designed in two stages, i.e., the upper and lower level control stages, as shown in Fig. 10. The upper level controller is composed of sideslip angle and yaw rate tracking controllers. At the lower level controller, it is composed of a control torque distribution algorithm and an electric power steering (EPS) motor controller.
3) Third, the sideslip angle observer based on the EKF approach is designed for providing accurate sideslip angle information to the stability controller. As explained in Section IV-B, a proposed EKF utilizes the estimated tire cornering stiffness and measured lateral tire forces. The RLS algorithm with a projection function is used to iteratively update the unknown parameters, i.e., the tire cornering stiffness and the estimated parameters are used to update the feedforward controller and as measurable state variables in EKF.

In this paper, we present the new control scheme, utilizing active front steering through an SbW system and independent in-wheel motor control, as a practical solution to the vehicle stability issues in an IWM-EV. A 2-DOF control method, which is widely applied in many motion control systems, is used to generate front steering angle and direct yaw moment to be controlled for stabilizing vehicle motion.

A. Desired Vehicle Model

The objective of stability control is to improve the vehicle steadiness and transient response properties, enhancing vehicle handling performance and maintaining stability in those cornering maneuvers, i.e., the yaw rate γ or sideslip angle β of the vehicle should be close to the desired vehicle responses (γ_d and β_d). The desired vehicle responses are defined based on the driver's cornering intention (e.g., drivers' steering command and vehicle speed). As usual, vehicle responses during steady-state cornering [i.e., $\dot{\beta} = \dot{\gamma} = 0$ in (8)] are used as desired vehicle responses. The desired vehicle sideslip angle and yaw rate for the given steering angle and vehicle speed are defined as follows:

$$\gamma_d = \left(\frac{\omega_\lambda}{s+\omega_\lambda}\right) \cdot \frac{1}{1+K_s v_x^2} \frac{v_x}{l} \cdot \delta_{\text{cmd}} \tag{31}$$

$$\beta_d = \left(\frac{\omega_\beta}{s+\omega_\beta}\right) \cdot \frac{1-\left(\frac{m l_f v_x^2}{2 l l_r C_r}\right)}{1+K_s v_x^2} \frac{l_r}{l} \cdot \delta_{\text{cmd}} \tag{32}$$

$$K_s = \frac{m(l_r C_r - l_f C_f)}{2 l^2 C_f C_r} \tag{33}$$

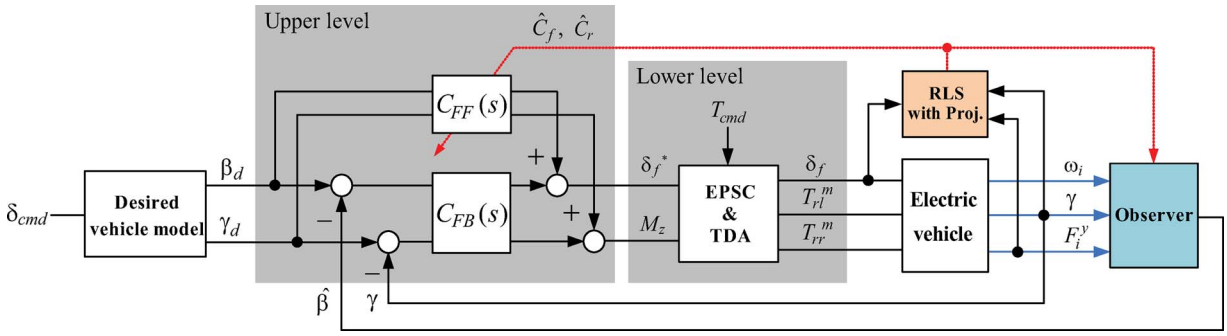

Fig. 10. Control structure of the proposed stability control system (EPSC: EPS controller. TDA: Torque distribution algorithm).

where ω_λ and ω_β are the cutoff frequencies (e.g., in this paper, 20 rad/s is chosen) of the desired model filters, respectively; and K_s is the vehicle stability factor, which explains the steering characteristics of the vehicles. The sign of $l_rC_r - l_fC_f$ in K_s represents the vehicle motion behavior by steering action, and the steering characteristics are classified as follows: 1) understeering $(l_rC_r - l_fC_f > 0)$; 2) neutral steering $(l_rC_r - l_fC_f = 0)$; and 3) oversteering $(l_rC_r - l_fC_f < 0)$.

B. Design of Feedforward and Feedback Controllers

In the proposed stability control system, the front steering angle δ_f and direct yaw moment M_z are used as controllable inputs. Front steering control is realized by an SbW system, including active EPS motor control. On the other hand, direct yaw moment control is realized by independent rear in-wheel motor control. Integrated control, which utilizes steering and driving torque control at the same time, was designed to satisfy the tracking performances of sideslip angle and yaw rate. Considering that a vehicle dynamics model, which is used in controller design, shows the time-varying characteristics due to varying parameters (e.g., tire cornering stiffness or vehicle speed), an adaptive feedforward controller is designed to handle those parameters.

In conventional 1-DOF controllers (e.g., proportional–integral–derivative controller, etc.), the only problem of the fixed robust controller is that the control performance of a closed-loop system becomes too conservative when the parameter variation in the vehicle model is too large. For this reason, an adaptive feedforward controller with parameter estimation is proposed to improve the tracking performance.

An adaptive feedforward controller is proposed based on real-time parameter adaptation, as described in Section IV-A. The adaptive feedforward controller is designed based on inverse vehicle dynamics (i.e., $G(s)$ is invertible) and given by

$$C_{\mathrm{FF}}(s) = \hat{B}^{-1}(sI - \hat{A}) = \begin{bmatrix} \hat{G}_{11} & \hat{G}_{12} \\ \hat{G}_{21} & \hat{G}_{22} \end{bmatrix} \tag{34}$$

where the elements of the feedforward controller $C_{\mathrm{FF}}(s)$ are described in Appendix A. Each element is updated based on the estimated tire cornering stiffness and the calculated vehicle speed. The average value of the nondriven wheel velocities is used for the vehicle speed. Considering that an electric vehicle used in field tests was a rear-wheel drive vehicle, it is reasonable to use the nondriven wheel's velocity as the vehicle speed. In case wheel slip occurs in the nondriven wheels due to sudden braking, we cannot use the nondriven wheel's velocity for calculating vehicle speed. In [30], the robust slip ratio estimation method was proposed and evaluated through experiments. If we know the wheel slip ratio, the vehicle speed can be easily calculated from the measured wheel velocity, regardless of acceleration and deceleration.

It is assumed that the open-loop plant can be stabilized by an appropriate feedback controller $C_{\mathrm{FB}}(s)$, taking account of closed-loop stability and disturbance rejection. In case of the vehicle plant, plant variation due to tire–road condition change (i.e., tire cornering stiffness) is large, and it makes control performances of the closed-loop system conservative. In feedback control design, a decoupling control method was applied to stabilize the vehicle lateral motion. Transfer functions between control inputs and outputs, shown in Appendix A, are interconnected with each other, and thereby, we have to compensate interconnection effects. The feedback controller $C_{\mathrm{FB}}(s)$ is designed as follows:

$$C_{\mathrm{FB}}(s) = \begin{bmatrix} C_\beta(s) & \rho_1(s)C_\gamma(s) \\ \rho_2(s)C_\beta(s) & C_\gamma(s) \end{bmatrix} \tag{35}$$

where $C_\beta(s)$ and $C_\gamma(s)$ are the proportional–integral compensator and are independently designed based on pole-placement interaction controllers, and $\rho_1(s)$ and $\rho_2(s)$ are selected based on a decoupling control method [36] and are given by

$$\rho_1(s) = -G_{11}(s)^{-1}G_{12}(s) \approx -G_{11}(0)^{-1}G_{12}(0) \tag{36}$$

$$\rho_2(s) = -G_{22}(s)^{-1}G_{21}(s) \approx -G_{22}(0)^{-1}G_{21}(0). \tag{37}$$

Here, the steady-state interconnection is only considered for avoiding complicated decoupling structures. This implies that a proposed interaction controller contributes to minimize the strong interconnection effects of the vehicle states to be controlled.

C. Design of EPSC and TDA

EPS motor control (under position control) is employed for realizing an SbW system. As shown in Fig. 11(a), the feedback controller $C_{\mathrm{EPS}}(s)$ is designed for the actual steering angle to track the reference front steering angle $\delta_f^\star$, which is generated from the upper controller. A constant feedback gain (i.e., proportional gain) was chosen to guarantee system bandwidth up

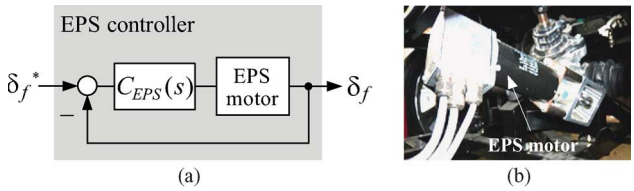

Fig. 11. EPS control system. (a) Block diagram of an EPSC. (b) EPS motor.

TABLE I
SPECIFICATIONS OF THE EXPERIMENTAL ELECTRIC VEHICLE

Total weight	875 kg
Wheel base	1.715 m
Track width	1.3 m
Yaw moment of inertia	617 kg·m^2
Spin inertia for each wheel	1.26 kg·m^2
In-wheel motor	PMSM (outer rotor type)
Max. Power	10.7 kW (for one rear motor)
Max. Torque	340 Nm (for one rear motor)
Max. Speed	1500 rpm
Controller	AutoBox-DS1103
Steering system	Steer-by-Wire
Suspension system	Double wishbone type
Battery	Lithium-ion

to 15 Hz. An EPS motor, as shown in Fig. 11(b), is a high-speed dc motor with 250-W power output.

The control yaw moment M_z, which is generated from an upper controller, is distributed to two rear in-wheel motors based on the following equations [7]:

$$M_z = \frac{d}{2}\left(F_{\mathrm{rr}}^x - F_{\mathrm{rl}}^x\right) \tag{38}$$

$$T_{\mathrm{cmd}} = T_{\mathrm{rr}}^m + T_{\mathrm{rl}}^m \tag{39}$$

where torque control commands to two rear in-wheel motors are calculated as $T_{\mathrm{rr}}^m = rF_{\mathrm{rr}}^x$ and $T_{\mathrm{rl}}^m = rF_{\mathrm{rl}}^x$, respectively. Note that, in this study, we have only utilized the rear in-wheel motors for controlling the yaw moment, and thereby, a simple torque distribution algorithm is applied. In future study, front in-wheel motors and novel control allocation algorithms [31]–[33] can be applicable to motion control systems of IWM-EVs to improve control flexibility and energy efficiency.

VI. SIMULATION AND EXPERIMENTAL RESULTS

A. Computer Simulation

Computer simulation was performed to evaluate the proposed stability control system. Based on the specifications of an experimental IWM-EV (see Table I), the simulation vehicle model was obtained using CarSim. A simulation environment using the CarSim model and Matlab/Simulink was constructed for the implementation of the proposed control algorithms. The proposed stability control system was evaluated through cosimulation for single-lane-change tests. Single-lane-change tests were carried out at $v_x = 70$ km/h on a low-μ road (i.e., $\mu \simeq 0.4$).

Fig. 12 shows the simulation results. Fig. 12(a) and (b) represents a control front steering angle and yaw moment. As

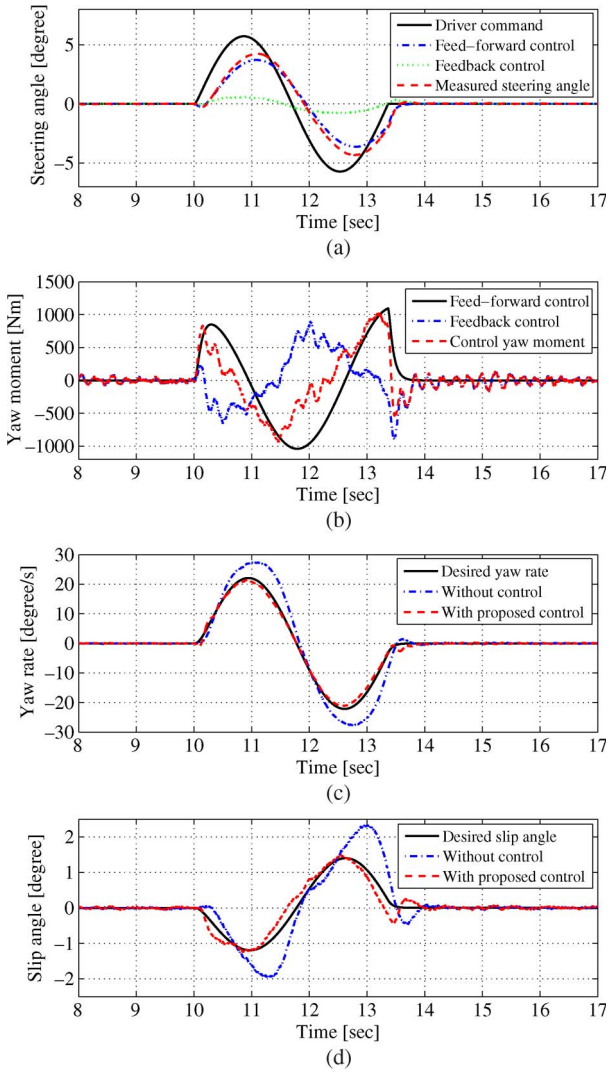

Fig. 12. Simulation results for single-lane change at $v_x = 70$ km/h. (a) Steering angle. (b) Yaw moment. (c) Yaw rate. (d) Sideslip angle.

shown in Fig. 12(d), if the control is set off, the vehicle sideslip angle increases, which causes the vehicles to lose stability and not accomplish the desired vehicle motion. By applying the proposed control algorithm, the yaw rate and sideslip angle are successfully controlled to follow the desired values with small errors.

B. Experimental Result

A proposed stability control algorithm is implemented on an experimental IWM-EV shown in Fig. 3. The single-lane-change maneuver has been done on dry asphalt (i.e., $\mu \simeq 0.9$). Fig. 13 shows the experimental results of an uncontrolled vehicle. The beginning of the first 6 s is the period of the acceleration to achieve a constant vehicle speed. A wheel steering command is given in the control algorithm, and an EPS motor controller has been activated by a driver to track the wheel steering command. On the other hand, yaw rate and sideslip angle controllers are not activated. From Fig. 13(a) and (b), we can see that an uncontrolled vehicle do not follow the desired vehicle trajectory

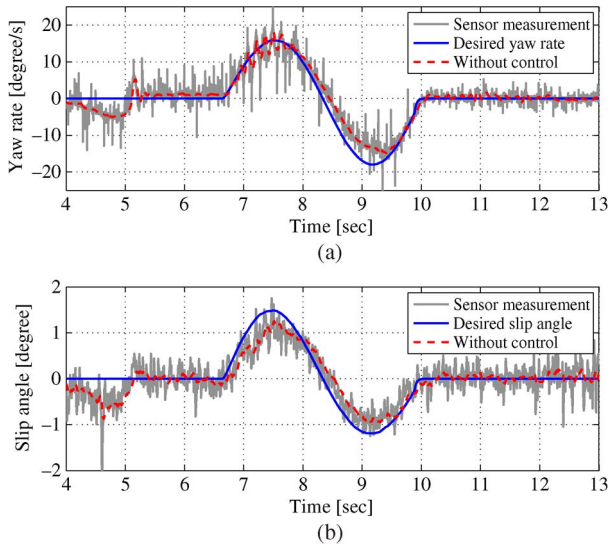

Fig. 13. Experimental results for an uncontrolled vehicle. (a) Yaw rate: without control. (b) Sideslip angle: without control.

(e.g., the maximum value of yaw rate and sideslip angle errors are about 7 $^\circ/$s and 0.75°).

With the same maneuver, experiments have been performed to evaluate the proposed stability control system. Fig. 14 shows the results of a controlled vehicle. Fig. 14(a) represents control flags, which imply the ON/OFF-states of the subcontrollers (i.e., yaw rate and sideslip angle control). At $t = 3.7$ s, control switches for yaw rate and sideslip angle control are turned on. Fig. 14(b) and (c) shows the control commands of the front steering angle and yaw moment to be controlled. The front steering angle is controlled to compensate a sideslip angle error, and the yaw moment is generated to compensate a yaw rate error, respectively. Fig. 14(d) and (e) shows the yaw rate and sideslip angle of a controlled vehicle with a proposed controller. The vehicle yaw rate with the proposed control, i.e., the thick red line in Fig. 14(d), is the filtered value of sensor measurement [i.e., the thick gray line in Fig. 14(d)]. As shown in Fig. 14(d), the vehicle yaw rate with the proposed control follows the desired yaw rate (i.e., dotted blue line). Similarly, the vehicle sideslip angle with the proposed control well tracks the desired trajectory with small error. If we compare results of the control case (see Fig. 14) and no-control case (see Fig. 13), we can confirm that the proposed stability control system is effective for guaranteeing the desired motion of the IWM-EV with an SbW system.

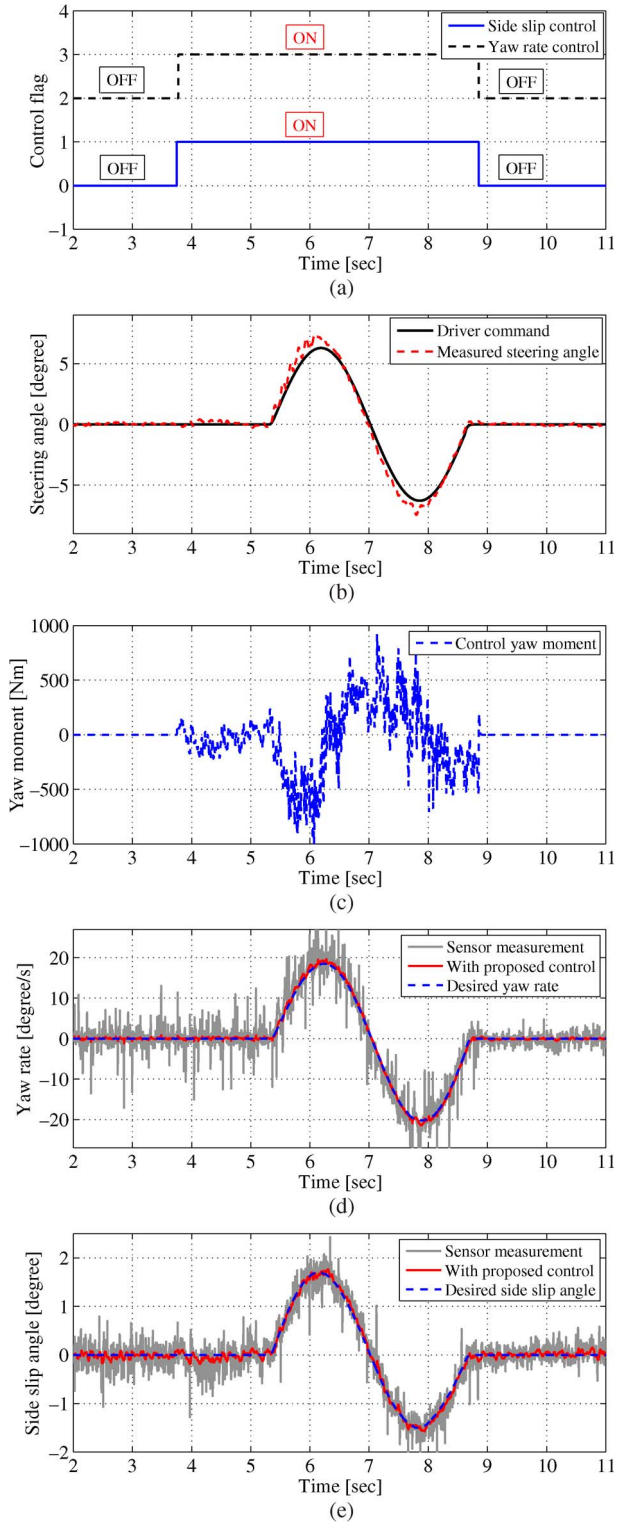

Fig. 14. Experimental results for a controlled vehicle. (a) Control flag. (b) Steering angle. (c) Yaw moment. (d) Yaw rate: with control. (e) Sideslip angle: with control.

VII. Conclusion and Future Works

This paper has presented a new method for sideslip angle estimation based on the practical use of lateral tire force sensors. A state observer, which is derived from EKF techniques, has been designed, and its estimation ability has been verified through experiments on an IWM-EV. Comparison with sideslip angle measured from the Correvit sensor has demonstrated the robustness and accuracy of the proposed observer. It is expected that the lateral tire force sensors, which were invented by NSK Ltd., are widely used in state estimation and motion control in the near future. The experimental verification of the practical application of lateral tire force sensors to vehicle control systems is one of the important results in this study. Based on the estimated sideslip angle, a lateral stability control system for an IWM-EV has been proposed,

and its performance has been investigated through CarSim-MATLAB/Simulink cosimulation and experiments. Simulation and experimental results have shown that the vehicle with the proposed stability control system, which is composed of active front steering and independent rear in-wheel motor control algorithms, can successfully follow the defined vehicle yaw rate and sideslip angle trajectories. Through robust motion control based on fast and accurate in-wheel motor control and robust estimation using lateral tire force sensors, lateral vehicle stability can be significantly enhanced. Since the proposed EKF is designed based on the linear dynamic tire model and the single-track vehicle model, some estimation errors may occur during severe driving on low-μ road. Therefore, in future works, we will improve the vehicle and tire models by taking into account road-bank angle, vehicle roll motion, and nonlinear tire characteristics.

APPENDIX A
DERIVATION OF SYSTEM TRANSFER FUNCTION

In this Appendix, transfer functions from inputs to outputs, which are obtained from a state-space representation (8), are derived. According to (8), the relationship between inputs and outputs is represented as follows:

$$\begin{bmatrix}\beta\\ \gamma\end{bmatrix} = \begin{bmatrix}G_{11}(s) & G_{12}(s)\\ G_{21}(s) & G_{22}(s)\end{bmatrix}\begin{bmatrix}\delta_f\\ M_z\end{bmatrix} = \Delta(s)\begin{bmatrix}G_{11}(0)(1+T_{11}s) & G_{12}(0)(1+T_{12}s)\\ G_{21}(0)(1+T_{21}s) & G_{22}(0)(1+T_{22}s)\end{bmatrix}\begin{bmatrix}\delta_f\\ M_z\end{bmatrix}$$

where $\Delta(s)$ is expressed as a second-order filter having damping coefficient ζ and natural frequency ω_n, i.e.,

$$\Delta(s) = \frac{\omega_n^2}{s^2 + 2\zeta\omega_n s + \omega_n^2}.$$

Here

$$\zeta = \frac{m\left(l_f^2 C_f + l_r^2 C_r\right) + I_z(C_f + C_r)}{2l\sqrt{mI_z C_f C_r\left(1 + K_s v_x^2\right)}}$$

$$\omega_n = \frac{2l}{v_x}\sqrt{\frac{C_f C_r\left(1 + K_s v_x^2\right)}{mI_z}}.$$

The dc gains and derivative gains in the aforementioned transfer functions are obtained as follows:

$$G_{11}(0) = \frac{l_r\left(1 - \frac{ml_f v_x^2}{2ll_r C_r}\right)}{l\left(1 + K_s v_x^2\right)},\ T_{11} = \frac{I_z v_x}{2ll_r C_r\left(1 - \frac{ml_f v_x^2}{2ll_r C_r}\right)}$$

$$G_{12}(0) = \frac{2(l_r C_r - l_f C_f) - mv_x^2}{4l^2 C_f C_r\left(1 + K_s v_x^2\right)},\ T_{12} = 0$$

$$G_{21}(0) = \frac{v_x}{l(1 + K_s v_x^2)},\ T_{21} = \frac{ml_f v_x}{2lC_r}$$

$$G_{22}(0) = \frac{(C_f + C_r)v_x}{2l^2 C_f C_r\left(1 + K_s v_x^2\right)},\ T_{22} = \frac{mv_x}{2(C_f + C_r)}.$$

APPENDIX B
KINEMATICS-BASED ESTIMATION METHOD

In this Appendix, a kinematics-based estimation method is explained. The lateral vehicle velocity is estimated using an RLS algorithm, and its estimate is used to finally calculate vehicle sideslip angle (i.e., $\beta = v_y/v_x$). To design the lateral vehicle velocity estimator, lateral tire force models are simplified from the following assumptions.

1) The lateral tire force is proportional to the tire slip angle.
2) Left and right tire cornering stiffnesses are the same (i.e., $C_{\mathrm{fl}} = C_{\mathrm{fr}} \approx C_f$).

From the preceding assumptions, the front lateral tire forces can be expressed as

$$F_{\mathrm{fl}}^y = -C_{\mathrm{fl}}\alpha_{\mathrm{fl}} \approx -C_f\left(\frac{v_y + \gamma l_f}{v_x - \gamma d/2} - \delta_f\right)$$

$$F_{\mathrm{fr}}^y = -C_{\mathrm{fr}}\alpha_{\mathrm{fr}} \approx -C_f\left(\frac{v_y + \gamma l_f}{v_x + \gamma d/2} - \delta_f\right).$$

From the aforementioned equations (by removing C_f), the lateral vehicle velocity v_y is derived as

$$v_y = \gamma l_f - \frac{\delta_f\left(F_{\mathrm{fl}}^y - F_{\mathrm{fr}}^y\right)}{\frac{F_{\mathrm{fl}}^y}{v_x + \gamma d/2} - \frac{F_{\mathrm{fr}}^y}{v_x - \gamma d/2}}.$$

Considering that all output data and input data are determined at sample instant, v_y described in the preceding equation can thus be formulated by the RLS algorithm, i.e.,

$$y(t) = \varphi^T(t)\theta(t)$$

where the estimated parameter $\theta(t)$, input regression $\varphi^T(t)$, and measured output $y(t)$ are given as

$$\theta(t) = v_y$$

$$\varphi^T(t) = \left(\frac{F_{\mathrm{fl}}^y}{v_x + \gamma d/2} - \frac{F_{\mathrm{fr}}^y}{v_x - \gamma d/2}\right)$$

$$y(t) = \gamma l_f\left(\frac{F_{\mathrm{fl}}^y}{v_x + \gamma d/2} - \frac{F_{\mathrm{fr}}^y}{v_x - \gamma d/2}\right) - \delta_f\left(F_{\mathrm{fl}}^y - F_{\mathrm{fr}}^y\right).$$

ACKNOWLEDGMENT

The authors would like to thank NSK Ltd., for providing MSHub units and technical support, and the Hori/Fujimoto Laboratory EV team colleagues for their help during the experiments.

REFERENCES

[1] Y. Hori, "Future vehicle driven by electricity and control-research on four-wheel-motored 'UOT Electric March II'," *IEEE Trans. Ind. Electron.*, vol. 51, no. 5, pp. 954–962, Oct. 2004.
[2] G. A. Magallan, C. H. D. Angelo, and G. O. Garcia, "Maximization of the traction forces in a 2WD electric vehicle," *IEEE Trans. Veh. Technol.*, vol. 60, no. 2, pp. 369–380, Feb. 2011.
[3] S. Sakai, H. Sado, and Y. Hori, "Motion control in an electric vehicle with four independently driven in-wheel motors," *IEEE/ASME Trans. Mechatronics*, vol. 4, no. 1, pp. 9–16, Mar. 1999.

[4] G. Cong, L. Mostefai, M. Denai, and Y. Hori, "Direct yaw-moment control of an in-wheel-motored electric vehicle based on body slip angle fuzzy observer," *IEEE Trans. Ind. Electron.*, vol. 56, no. 5, pp. 1411–1419, May 2009.
[5] K. Kim, S. Hwang, and H. Kim, "Vehicle stability enhancement of four-wheel-drive hybrid electric vehicle using rear motor control," *IEEE Trans. Veh. Technol.*, vol. 57, no. 2, pp. 727–735, Mar. 2008.
[6] J. Kim, C. Park, S. Hwang, Y. Hori, and H. Kim, "Control algorithm for an independent motor-drive vehicle," *IEEE Trans. Veh. Technol.*, vol. 59, no. 7, pp. 3213–3222, Sep. 2010.
[7] H. Fujimoto, A. Tsumasaka, and T. Noguchi, "Direct yaw-moment control of electric vehicle based on cornering stiffness estimation," in *Proc. IEEE IECON*, Nov. 2005, pp. 2626–2631.
[8] D. Piyabongkarn, R. Rajamani, J. Grogg, and J. Lew, "Development and experimental evaluation of a slip angle estimator for vehicle stability control," *IEEE Trans. Control Syst. Technol.*, vol. 17, no. 1, pp. 78–88, Jan. 2009.
[9] H. F. Grip, L. Imsland, T. A. Johansen, J. C. Kalkkuhl, and A. Suissa, "Vehicle sideslip estimation," *IEEE Control Syst. Mag.*, vol. 29, no. 5, pp. 36–52, Oct. 2009.
[10] M. Doumiati, A. C. Victorino, A. Charara, and D. Lechner, "Onboard real-time estimation of vehicle lateral tire-road forces and sideslip angle," *IEEE/ASME Trans. Mechatron.*, vol. 16, no. 4, pp. 601–614, Aug. 2011.
[11] A. von Vietinghoff, M. Hiemer, and U. Kiencke, "Nonlinear observer design for lateral vehicle dynamics," in *Proc. IFAC World Congr.*, Prague, Czech Republic, 2005, pp. 988–993.
[12] M. Hiemer, A. von Vietinghoff, U. Kiencke, and T. Matsunaga, "Determination of the vehicle body slip angle with non-linear observer strategies," presented at the SAE World Congr., Detroit, MI, 2005, Paper 2005-01-0400.
[13] D. M. Bevly, J. Ryu, and J. C. Gerdes, "Integrating INS sensors with GPS measurements for continuous estimation of vehicle sideslip, roll, and tire cornering stiffness," *IEEE Trans. Intell. Transp. Syst.*, vol. 7, no. 4, pp. 483–493, Dec. 2006.
[14] R. Daily and D. M. Bevly, "The use of GPS for vehicle stability control systems," *IEEE Trans. Ind. Electron.*, vol. 51, no. 2, pp. 270–277, Apr. 2004.
[15] B. A. Guvenc, L. Guvenc, and S. Karaman, "Robust yaw stability controller design and hardware-in-the-loop testing for a road vehicle," *IEEE Trans. Veh. Technol.*, vol. 58, no. 2, pp. 555–571, Feb. 2009.
[16] K. Nam, Y. Kim, S. Oh, and Y. Hori, "Steering angle-disturbance observer(SA-DOB) based yaw stability control for electric vehicles with in-wheel motors," in *Proc. ICCAS*, Dec. 2010, pp. 1303–1307.
[17] Y. Yamaguchi and T. Murakami, "Adaptive control for virtual steering characteristics on electric vehicle using steer-by-wire system," *IEEE Trans. Ind. Electron.*, vol. 56, no. 5, pp. 1585–1594, May 2009.
[18] H. Ohara and T. Murakami, "A stability control by active angle control of front-wheel in a vehicle system," *IEEE Trans. Ind. Electron.*, vol. 55, no. 3, pp. 1277–1285, Mar. 2008.
[19] J. Ahmadi, A. K. Sedigh, and M. Kabganian, "Adaptive vehicle lateral-plane motion control using optimal tire friction forces with saturation limits consideration," *IEEE Trans. Veh. Technol.*, vol. 58, no. 8, pp. 4098–4107, Sep. 2009.
[20] Y. Yamauchi and H. Fujimoto, "Vehicle motion control method using yaw-moment observer and lateral force observer for electric vehicle," *IEEJ Trans. Ind. Appl.*, vol. 130, no. 8, pp. 939–944, 2010.
[21] H. Fujimoto and B. Yao, "Multirate adaptive robust control for discrete-time non-minimum phase systems and application to linear motors," *IEEE/ASME Trans. Mechatronics*, vol. 10, no. 4, pp. 371–377, Aug. 2005.
[22] H. Sado, S. Sakai, and Y. Hori, "Road condition estimation for traction control in electric vehicle," in *Proc. IEEE ISIE*, Jul. 1999, pp. 973–978.
[23] R. Rajamani, G. Phanomchoeng, D. Piyabongkarn, and J. Y. Lew, "Algorithms for real-time estimation of individual wheel tire-road friction coefficients," *IEEE/ASME Trans. Mechatron.*, 2011, DOI: 10.1109/TMECH.2011.2159240, to be published.
[24] K. Nam, S. Oh, H. Fujimoto, and Y. Hori, "Vehicle state estimation for advanced vehicle motion control using novel lateral tire force sensors," in *Proc. Amer. Control Conf.*, San Francisco, CA, 2011, pp. 4853–4858.
[25] K. Nam, S. Oh, H. Fujimoto, and Y. Hori, "Estimation of sideslip and roll angles of electric vehicles using lateral tire force sensors through RLS and Kalman filter approaches," *IEEE Trans. Ind. Electron.*, DOI: 10.1109/TIE.2012.2188874, to be published.
[26] C. Sierra, E. Tseng, A. Jain, and H. Peng, "Cornering stiffness estimation based on vehicle lateral dynamics," *Veh. Syst. Dyn.*, vol. 44, no. Suppl., pp. 24–38, 2006.
[27] B. M. Nguyen, K. Nam, H. Fujimoto, and Y. Hori, "Proposal of cornering stiffness estimation without vehicle side slip angle using lateral force sensor," in *Proc. IEEJ Technical Meeting Record*, 2011, vol. IIC-11-140, pp. 37–42.
[28] H. Imine, N. K. M'Sirdi, and Y. Delanne, "Sliding mode observers for systems with unknown inputs: Application to estimating the road Profile," in *Proc. IMechE. Part D, J. Automobile Eng.*, Aug. 2005, vol. 219, no. 8, pp. 989–997.
[29] H. Imine, N. K. M'Sirdi, and Y. Delanne, "Adaptive observers and estimation of the road profile," presented at the SAE World Congr. Exhib., Detroit, MI, Mar., 2003, Paper 2003-01-1282.
[30] T. Suzuki and H. Fujimoto, "Slip ratio estimation and regenerative brake control for decelerating electric vehicles without detection of vehicle velocity and acceleration," *IEEJ Trans. Ind. Appl.*, vol. 130, no. 4, pp. 512–517, 2010.
[31] M. Jonasson, J. Andreasson, S. Solyom, B. Jacobson, and A. S. Trigell, "Utilization of actuators to improve vehicle stability at the limit: From hydraulic brakes toward electric propulsion," *J. Dyn. Sys., Meas., Control*, vol. 133, no. 5, p. 051003, Sep. 2011.
[32] J. Tjonnas and T. A. Johansen, "Stabilization of automotive vehicles using active steering and adaptive brake control allocation," *IEEE Trans. Control Syst. Technol.*, vol. 18, no. 3, pp. 545–558, May 2010.
[33] Y. Chen and J. Wang, "Energy-efficient control allocation with applications on planar motion control of electric ground vehicles," in *Proc. Amer. Control Conf.*, San Francisco, CA, 2011, pp. 2719–2724.
[34] R. Rajamani, *Vehicle Dynamics and Control*. New York: Springer-Verlag, 2005.
[35] L. Ljung, *System Identification: Theory for the User*. Englewood Cliffs, NJ: Prentice–Hall, 1987.
[36] S. Skogestad and I. Postlethwaite, *Multivariable Feedback Control-Analysis and Design*. Hoboken, NJ: Wiley, 2005.
[37] K. Ono, T. Takizawa, and M. Aoki, "Preload measuring device for double row rolling bearing unit," U.S. Patent 20 090 052 825A1, Feb. 26, 2009.

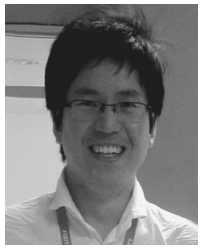

Kanghyun Nam (S'10) received the B.S. degree in mechanical engineering from Kyungpook National University, Daegu, Korea, in 2007 and the M.S. degree in mechanical engineering from the Korea Advanced Institute of Science and Technology, Daejeon, Korea, in 2009. He is currently working toward the Ph.D. degree in electrical engineering with the Department of Electrical Engineering, Graduate School of Engineering, The University of Tokyo, Tokyo, Japan.

During 2008–2009, he was a Control Engineer with the Advanced Brake System R&D Center, MANDO Corporation, Gunpo, Korea. His research interests include vehicle dynamics and control, state estimation and motion control for electric vehicles, and robust control.

Mr. Nam is a Member of the Society of Automotive Engineers of Japan and the Korean Society of Automotive Engineers.

Hiroshi Fujimoto (S'99–M'01) received the Ph.D. degree from The University of Tokyo, Tokyo, Japan, in 2001.

In 2001, he joined the Department of Electrical Engineering, Nagaoka University of Technology, Niigata, Japan, as a Research Associate. From 2002 to 2003, he was a Visiting Scholar with the School of Mechanical Engineering, Purdue University, West Lafayette, IN. In 2004, he joined the Department of Electrical and Computer Engineering, Yokohama National University, Yokohama, Japan, as a Lecturer, and he became an Associate Professor in 2005. He has been an Associate Professor with the Department of Advanced Energy, Graduate School of Frontier Sciences, The University of Tokyo, since 2010. His research interests include control engineering, motion control, nanoscale servo systems, electric vehicle control, and motor drives.

Dr. Fujimoto is a Member of the Institute of Electrical Engineers of Japan, the Society of Instrument and Control Engineers (SICE), the Robotics Society of Japan, and the Society of Automotive Engineers of Japan. He received the Best Paper Award from the IEEE TRANSACTION ON INDUSTRIAL ELECTRONICS in 2001, the Isao Takahashi Power Electronics Award in 2010, and the Best Author Prize from the SICE in 2010.

Yoichi Hori (S'81–M'83–SM'00–F'05) received the B.S., M.S., and Ph.D. degrees in electrical engineering from The University of Tokyo, Tokyo, Japan, in 1978, 1980, and 1983, respectively.

In 1983, he joined the Department of Electrical Engineering, The University of Tokyo, as a Research Associate, where he later became an Assistant Professor, an Associate Professor, and, in 2000, a Professor. He moved to the Institute of Industrial Science as a Professor with the Information and System Division in 2002 and to the Department of Advanced Energy, Graduate School of Frontier Sciences, The University of Tokyo, in 2008. From 1991 to 1992, he was a Visiting Researcher with the University of California, Berkeley. His research interests are control theory and its industrial applications to motion control, mechatronics, robotics, electric vehicles, etc.

Dr. Hori has been the Treasurer of the IEEE Japan Council and Tokyo Section since 2001. He is also an Administrative Committee member of the IEEE Industrial Electronics Society and a member of the Society of Instrument and Control Engineers, the Robotics Society of Japan, the Japan Society of Mechanical Engineers, and the Society of Automotive Engineers of Japan (JSAE). He was the President of the Industry Applications Society of the Institute of Electrical Engineers of Japan (IEEJ), the President of Capacitors Forum, the Chairman of the Motor Technology Symposium of the Japan Management Association, and the Director on Technological Development of JSAE. He received the Best Transactions Paper Award from the IEEE TRANSACTION ON INDUSTRIAL ELECTRONICS in 1993 and 2001, the 2000 Best Transactions Paper Award from the IEEJ, and the 2011 Achievement Award from the IEEJ.